Journal Pre-proofs

Susceptibility of X17CrNi16-2 martensitic stainless steel to hydrogen embrittlement after conventional and deep cryogenic heat treatment

Mirjam Bajt Leban, Bojan Zajec, Bojan Podgornik, Črtomir Donik, Patricia Jovičević-Klug, Miha Hren, Andraž Legat

Please cite this article as: Leban, M.B., Zajec, B., Podgornik, B., Donik, C., Jovičević-Klug, P., Hren, M., Legat, A., Susceptibility of X17CrNi16-2 martensitic stainless steel to hydrogen embrittlement after conventional and deep cryogenic heat treatment, *Engineering Failure Analysis* (2024), doi: https://doi.org/10.1016/j.engfailanal.2024.108403

Susceptibility of X17CrNi16-2 martensitic stainless steel to hydrogen embrittlement after conventional and deep cryogenic heat treatment

Mirjam Bajt Leban[1]*, Bojan Zajec[1], Bojan Podgornik[2], Črtomir Donik[2], Patricia Jovičević-Klug[3], Miha Hren[1], Andraž Legat[1]

[1] Slovenian National Building and Civil Engineering Institute, Dimičeva 12, 1000 Ljubljana, Slovenia

[2] Institute of Metals and Technology, Lepi pot 11, 1000 Ljubljana, Slovenia

[3] Max-Planck-Institut für Eisenforschung GmbH, Max-Planck-Straße 1, 40237 Düsseldorf, Germany

Abstract

A low carbon/ high chromium martensitic stainless steel, X17CrNi16-2, was heat treated using two different hardening and tempering regimes (1050 °C/480 °C or 980 °C/600 °C) — promoting either a high strength or high toughness state, respectively - and further combined with deep cryogenic treatment (DCT) at -196 °C for 24 h. Over recent years DCT has been recognized as a promising technique to improve the properties of steel, predominantly with respect to its tensile strength, toughness and wear resistance. The influence of DCT on the hydrogen embrittlement resistance of martensitic stainless steel has not yet, however, been reported.

A slow strain rate tensile test (SSRT) with simultaneous cathodic hydrogen charging was selected as the method to assess potential susceptibility to hydrogen embrittlement (HE). Relatively low-intensity hydrogen charging, utilizing a constant current density of 0.1 mA/cm², in a non-corrosive, slightly alkaline buffer solution, led to a clear reduction in the ultimate tensile stress. This reduction, and therefore the HE susceptibility, was more pronounced in the steel with a higher strength (i.e. that subject to the 1050 °C/ 480 °C heat treatment condition). Furthermore, DCT did not appear to have any impact on the steel's mechanical properties in the presence of hydrogen. Fractographic analysis showed clear evidence of HE in the hydrogen-charged specimens.

This paper presents results of the SSRT tests and further fractography results, and discusses the impact of conventional and deep cryogenic treatment on HE susceptibility.

Keywords: martensitic stainless steel, deep cryogenic treatment, hydrogen embrittlement, slow strain rate tensile test

1. Introduction

Martensitic stainless steels (MSS) are a class of martensitic steels with a high Cr content, which provides resistance against corrosion. This, in combination with their favourable mechanical properties, allows them to be used in demanding environments. These steels are used in a wide variety of fields, including the automotive, renewable, and nuclear energy sectors, the petrochemical industry, and many others [1]. Martensitic steels obtain their mechanical properties through heat treatment, which consists of two main phases: austenitization followed by quenching, and tempering [2]. The latter involves reheating the steel to a specific temperature range, followed by controlled cooling. Tempering improves the ductility and toughness of the material by refining the microstructure and relieving internal stresses. Additionally, tempering mitigates the brittleness associated with the

as-quenched state, enhancing the overall mechanical properties of the material. The controlled transformation of retained austenite (RA) plays a crucial role in balancing the combination of hardness and toughness, thus optimizing the steel for a diverse range of applications.

Over recent years, deep cryogenic treatment (DCT) has gained attention as a promising modification to conventional heat treatments (CHT) in a number of different alloys. During this type of treatment, the material is exposed to sub-zero temperatures, which cause changes in the microstructure of the metal; in the case of stainless steels, the most obvious change is the reduction in RA, caused by its transformation to martensite [3]. The improvement in the mechanical, fatigue, and wear properties of steels obtained through DCT has traditionally been attributed to the transformation of RA into martensite [4] and the refinement of secondary carbides [5]. Recent studies, however, have also shown the importance of the deformation of martensite during martensitic transformation at low temperatures [6]. Furthermore, compressive strains are generated in austenite following the transformation of martensite at low temperatures, which subsequently influences the stability of austenite during the tempering phase [7].

The primary reason for the cryogenic treatment of martensitic stainless steels is to reduce RA, because RA is metastable and can easily transform into brittle martensite, thus leading to a deterioration in the properties of the material. Cryogenic treatment effectively reduces the levels of RA from 20-30% to less than 2% [8,9]. In addition to reducing the amount of RA, DCT has also been found to accelerate the precipitation of small globular carbides during tempering [10], austenite retransformation [11], and overall microstructural refinement [8,11]. After DCT, martensitic stainless steels typically show increased levels of hardness (up to 40 %), strength, and ductility (up to 25%) [9], although this is at the expense of toughness and fatigue resistance, both of which reduce. This is mostly due to increased carbide growth at the grain boundaries and a significant reduction in the austenite phase [11].

MSSs are generally considered as high-strength steels, having an ultimate tensile strength (UTS) of above 1000 MPa. As such, they are susceptible to hydrogen embrittlement (HE). HE in steels is a phenomenon that occurs when atomic hydrogen diffuses through a solid metal lattice, localizes around crystal imperfections (vacancies, dislocations, grain boundaries, precipitates, inclusions, interfaces, etc.) [12], and then interacts with the metal lattice structure, leading to a loss in ductility and ultimately causing the material to become brittle [13]. Various studies have shown that only diffusive hydrogen is responsible for HE, with any H atoms trapped in deep (irreversible) traps not contributing to the phenomenon [14]. Multiple phenomena are involved in this process, including hydrogen dissolution, hydrogen diffusion, hydrogen redistribution, and hydrogen interactions with crystal imperfections. Consequently, several hydrogen embrittlement mechanisms have been successively identified to explain the phenomena of HE [15–17]. Of these, the two mechanisms most likely to cause HE failure of high-strength MSS are hydrogen-induced decohesion and hydrogen-induced plasticity [15,18].

HE presents a significant challenge in various industrial sectors; in the automotive, aerospace and oil and gas industries, where high-strength steels are commonly used. HE is a particularly elusive form of material degradation, as no discernible signs are evident with its onset and it cannot be detected either visually or by any other simple method. Moreover, structural failure often occurs with a certain delay, following interaction between the steel and hydrogen. The mechanisms underlying hydrogen embrittlement are complex and multifaceted, involving factors such as hydrogen diffusion, trapping, and interaction with lattice defects [19], and, despite extensive research efforts, are still not well understood.

The ability to understand and mitigate hydrogen embrittlement is crucial for ensuring the reliability and safety of structural components subjected to hydrogen exposure, making it a topic of ongoing investigation.

2

In general, austenite has significantly higher solubility and lower diffusivity for hydrogen in comparison to martensite. The austenite phase thus represents a high-capacity hydrogen trap, which is often irreversible. When finely dispersed, such traps decrease the amount of diffusible hydrogen and impede its movement, therefore decreasing the effective hydrogen diffusion coefficient [20]. On the other hand, however, under sufficient stress or strain the RA can transform into fresh martensite. This alteration at the microstructural level can significantly influence the resistance of steel to hydrogen embrittlement.

The following section presents a short review of relevant studies recently conducted on hydrogen embrittlement in martensitic steels and martensitic stainless steels, with a predominant focus on the role of RA. Bacchi et al. [21] studied 16Cr5NiMo super martensitic stainless steel treated at three different tempering temperatures, leading to RA contents ranging between 0 and 15%. While the permeation tests revealed the effective hydrogen diffusion coefficient to be a decreasing function of the austenitic phase fraction, the embrittlement effect was found not to strictly correlate with the amount of RA, but rather to the large size of the prior austenitic grain [21].

Similarly, Lovicu et al. [22] studied martensitic quench and partitioning (Q&P) and quenched and tempered (Q&T) steels with identical chemical compositions and similar strengths, but the former contained 17.5% RA, while the latter contained less than 1%. After cathodic charging under identical conditions, the normalized thermal desorption spectra showed a single peak in both steels at almost the same temperature, indicating that RA does not act as a deep trapping site in that particular steel. As the hydrogen concentration increases, the mechanical properties deteriorated faster in the Q&P steel compared to in the Q&T steel. Interestingly, the reduction of UTS with increasing H content was very low in the Q&T steel, while its ductility was greatly reduced. Yang et. al. [23] reported that RA in Q&P steel retards diffusion and increases the solubility of hydrogen, thus contributing to the increase in HE resistance.

It has also been reported in the literature [24] that an increased tempering temperature during Q&T reduces the dislocation density [14,25]. The results of this study indicated that Cr-rich M_7C_3 carbides had an adverse impact on the HE resistance of tempered martensitic steel. It was also found that, in addition to RA, carbides also increase the solubility of H [26]. Austenite is a metastable phase in martensitic steels, which might transform to martensite under stress-strain and hydrogen attack. This transformation, however, depends upon the chemical composition, governed by the stacking fault energy (SFE) – the lower the SFE, the higher the susceptibility to transformation [27]. The presence of hydrogen can also decrease SFE [28]. RA reduces the susceptibility to HE, as RA is a hydrogen trap [27]. During deformation, RA can transform into strain-induced martensite, which plays an important role in the hydrogen-assisted fracture of metastable austenitic stainless steels in hydrogen [29].

Conclusions about the impact of RA on HE do, however, vary significantly: some authors report that RA has a detrimental effect on HE [26], while certain studies suggest a beneficial outcome [30], and others indicate little to no effect at all [21].

The main aim of this research was to investigate the influence of DCT, which is known to reduce RA in MSS, on HE, and to compare the effect with that on steel subjected to CHT. To investigate this, a slow strain rate test (SSRT) was conducted during non-intensive hydrogen charging. In addition to the analysis of mechanical properties, post-examination of the fractured specimens was conducted using scanning electron microscopy (SEM), back-scatter diffraction (EBSD), and microtomography.

2. Materials and methods

The material used in the present investigation was commercial X17CrNi16-2 martensitic stainless steel. The chemical composition of the material, as analyzed by optical emission spectroscopy, is given in Table 1.

Table 1: Chemical composition of the X17CrNi16-2 martensitic stainless steel. All results are reported in weight *%* [11]

	%C	%Si	%Cr	%Mn	%Ni	%S	%Cu	%Mo	%N
X17CrNi16-2	0.17	0.29	15.2	0.83	1.5	0.017	0.19	0.11	0.02

Four different heat treatments, consisting of austenitizing, tempering, and DCT, were applied on X17CrNi16-2 steel samples from a single batch and named E1 – E4. E1 and E2 were subjected to high austenitizing and low tempering temperatures, in order to target high hardness and tensile strength values, while low austenitizing and high tempering temperatures were used for E3 and E4, in order to produce better toughness. Each conventional heat treatment group (E1 and E3) was matched with a corresponding heat treatment regime including DCT (E2 and E4), which was performed immediately after quenching (and before tempering) by submerging the specimens in liquid nitrogen at -196°C for 24h. The main details concerning the heat treatment procedures, the basic properties obtained (hardness, tensile strength and fracture toughness) and the RA and carbide volume fractions are summarized in Table 2, while other experimental details related to the heat treatment and properties were reported by Jovičević-Klug et. al. [3,11].

Table 2: Heat treatment and main properties of the martensitic stainless steel samples investigated [11]

	E1		E2		E3	E4
	Final	Quenched	Final	DCT		
Austenitizing (^{o}C/min)	1050/30	1050/30	1050/30	1050/30	980/30	980/30
DCT (^{o}C/h)	-/	-/	-196/24	-196/24	/	-196/24
Tempering (^{o}C/h)	1x480/2	-/	1x480/2	-/	1x600/2	1x600/2
Hardness (HRC)	46.0		47.1		29.8	28.8
Tensile strength* (MPa)	1525		1589		1010	970
Fracture toughness (MPa√m)	73.8		29.1		82.7	77.7
% RA	15	3.5	1	1	2	<1
Carbides (vol.%)	$(Cr, Fe)_3C_2$ 3	2	3	1.5	4.5	6.5
	$(Cr, Fe)2_3C_6$ 20	<1	22	<1	12.5	13

*conventional tensile test at room temperature in the air according to SIST EN ISO 6892-1

The microstructural features of the steel investigated, as well as the influence of DCT on the microstructure and RA, have recently been published in two extensive papers by Jovičević-Klug et. al. [3,11] and are therefore only briefly summarised here. On average, martensitic laths were 50% coarser after the first type of heat treatment process (specimens E1 and E2), with the second set (E3 and E4) also showing a denser carbide population, particularly at the grain boundaries. Furthermore, much larger carbides, a stronger carbide enrichment and a reduced (~40% lower) volume fraction of $M_{23}C_6$ carbides were observed in the second group. Specimens E2 and E4, which were subjected to DCT, consisted of smaller martensitic laths and showed an enhanced precipitation of finer carbides in comparison to the CHT specimens E1 and E3. Carbide growth at the grain boundaries was, however, also detected in the DCT specimens (E2 and E4). The amount of RA in the steels subjected to DCT (1% and <1% for E2 and E4, respectively) was lower than that of the steels that were treated conventionally (15% and 2% for E1 and E3, respectively). The reduction in RA that occurred when steels were subjected to DCT treatment was significantly higher in the case of the first heat treatment, which consisted of a high austenitizing temperature and a low tempering temperature. A schematic

representation showing the evolution of the microstructure during DCT and CHT, alongside a detailed explanation and discussion, has been presented in previous research [11].

The impact of hydrogen charging on the mechanical properties of the steel was investigated by a slow strain rate tensile (SSRT) test, with multiple cylindrical specimens tested for each of the four heat treatments, E1 – E4. Cylindrical tensile specimens with a rounded V-shaped notch on the gauge length were manufactured on the lathe from a block of heat-treated steel. The dimensions of the specimens are given in Figure 1.
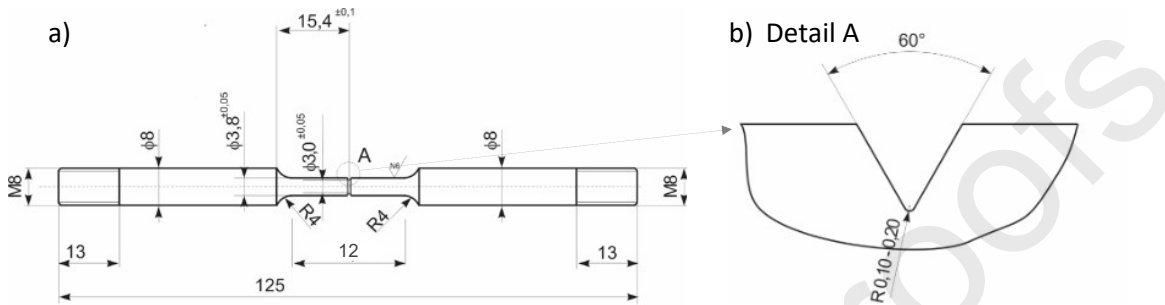

Figure 1: Dimensions of the SSRT tensile specimen (a) with a V-notch (b)

Cathodic hydrogen charging commenced simultaneously with the SSRT, which was conducted at room temperature (23 ± 1°C). After preliminary tests on the E1 specimens at higher current densities, which resulted in very low ultimate tensile strength values, it was decided to proceed with galvanostatic charging at a cathodic current of 0.1 mA/cm². Cathodic charging was carried out using a Gill AC potentiostat, conducted in a custom-made corrosion cell with a large-area Pt counter electrode surrounding the tensile specimen gauge section. The bottom part of the tensile specimen was sealed to the corrosion cell, while the top part was free to move due to elongation. Only the central part of the specimen, encompassing the entire section between the specimen shoulders, was exposed to the electrolyte. The electrolyte used for cathodic hydrogen charging was a slightly alkaline buffer solution, consisting of 4.77 g/L $Na_2B_4O_5(OH)_4 \cdot 10H_2O$ and 0.732 g/L NaOH. No corrosive species were added, so as to avoid the occurrence of any other form of corrosion during the exposure. Hydrogen bubbles that formed at the sample surface due to recombination were not removed, as the solution was stationary in the corrosion cell. The strain rate of the SSRT was 10^{-6}/s, which resulted in a cross-head displacement rate of 12 nm/s for a 12 mm gauge length. Following fracture of the specimen, the straining and cathodic charging were automatically switched off. The specimen may have then remained in the electrolyte for several more hours before being unmounted, rinsed in deionized water and dried. This non-aggressive solution did not cause any further corrosion or alteration in the stainless steel investigated. To fully confirm that the solution itself had no meaningful impact (e.g. stress corrosion cracking), one specimen was tested in the solution without polarization (i.e. no H charging). The results for this trial were identical to those for the specimens tested in the air. To serve as a reference, two specimens from each heat treatment procedure underwent the same SSRT test conducted in the air (i.e. no cathodic charging in the electrolyte).

Electron-backscatter diffraction (EBSD) measurements were conducted using a Zeiss CrossBeam 550 focused ion beam scanning electron microscope (FIB-SEM) fitted with an EDAX Hikari Super EBSD camera. EBSD post-processing was carried out using APEX and OIM 8.6 software. SE images were obtained using an accelerating voltage of 15 kV and a 2.0 nA probe current. EBSD analyses were performed on samples tilted at 70°, using a 10 nA probe current and a step size of 0.5 mm. The crystallographic grain orientations are depicted on inverse pole figure (IPF) and image quality (IQ)

6

maps, with different colors representing the orientation of a specific sample direction within a crystal frame.

The presence of cracks in the vicinity of the final fracture was investigated by the microCT technique using an Xradia MicroXCT-400 device. Tomography scans were conducted at a source voltage of 100 kV and power of 10 W power, using a 4x magnification objective and taking 1601 images across a 360° rotation. A single X-ray image had an exposure time of 15 seconds. A resolution of 4.19 μm was obtained, meaning that any cracks with an opening larger than 10 μm were accurately detected.

3. Results and discussion
3.1. Mechanical tests

Results from the SSRT test, including the tensile strength and elongation at break, both in the air and during hydrogen charging, are presented in Table 3 for each of the heat treatments investigated. For each heat treatment, two specimens were tested in the air and three tested with simultaneous hydrogen charging (with the exception of E1, where only two specimens were tested successfully). Stress-elongation curves for selected tensile specimens from each heat treatment group (both H-charged and air-tested) are presented in Figure 2. It is worth pointing out that results of the SSRT differ from results of the conventional tensile tests (presented in Table 2) due to differences in the strain rates and specimen shape.

It is evident from the stress-elongation curves depicted in Figure 2, and the outcomes presented in Table 3, that the tensile strength and elongation of specimens E1 and E2 are significantly higher than those of specimens E3 and E4 when tested in the air. This is mainly due to the lower tempering temperature, which resulted in a less tempered martensite matrix with higher hardness levels and a greater volume fraction of $M_{23}C_6$ carbides. Comparing the first set of specimens (E1 and E2), which were heat treated at high austenitizing and low tempering temperatures, it can be seen that DCT treatment (E2) slightly increases the mechanical properties following the SSRT test, as was expected due to the reduction in RA. On the other hand, the opposite trend was observed with respect to the tensile strength and elongation of specimens E3 and E4 when following the SSRT test in the air, with the material exposed to CHT (E3) exhibiting slightly better mechanical properties than E4. This is related to the finer martensitic laths and the enhanced and finer precipitation of carbides that becomes predominant at low tempering temperatures, as well as the enhanced precipitation of carbides at the grain boundaries.

During hydrogen charging, the mechanical properties of all the specimens tested were significantly reduced. This reduction is significantly greater in materials E1 and E2. The materials E1 and E2 exhibit a very high UTS in air and hydrogen charging therefore causes a severe reduction in their mechanical properties. It has been reported in the literature [31,32] that alloys with a higher strength are more susceptible to HE than those with a lower strength. A higher dislocation density and a greater amount of defects in the lattice could lead to higher HE sensitivity. Deleterious effect of hydrogen is less pronounced in materials E3 and E4, with the UTS values in air being lower. DCT treatment does not, however, appear to either improve or worsen the mechanical properties of the hydrogen-charged specimens in comparison to the corresponding CHT-treated specimens.
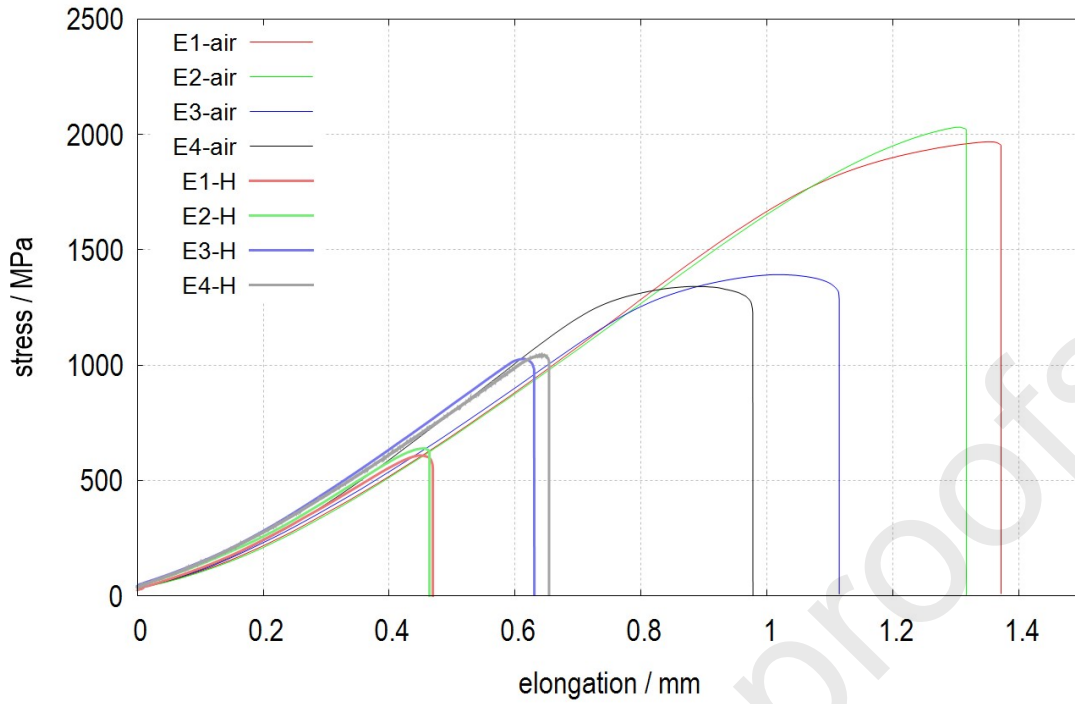
7

Figure 2: Stress–elongation (displacement) curves for selected SSRT tests conducted in the air (thinner lines) and during hydrogen charging at a current density of 0.1 mA/cm^2 (thicker lines)

A common way to quantify the susceptibility of a material to HE is the so-called dimensionless hydrogen embrittlement index (HEI), as calculated by equation (1) [33],

$$HEI = \frac{(\emptyset_{f,F} - \emptyset_{f,H})}{\emptyset_{f,F}}$$ (1)

where

$\emptyset_{f,F}$ is the result of the property (*f* = force – *F* or elongation – *l*) obtained during the SSRT in air and

$\emptyset_{f,H}$ is the result of the property (*f* = force – *F* or elongation – *l*) obtained during the SSRT under the hydrogen-charging condition.

It can be observed from Table 3 that the HEI values calculated from the tensile forces at fracture are significantly higher in materials E1 and E2 compared to in E3 and E4. The HEI calculated for elongation shows a slightly smaller difference between the two groups of materials. There was no significant difference between the HEI results of materials subjected to CHT and DCT in either of the basic heat treatment groups.

Table 3: Tensile properties and HEI calculated for specimens tested in the air and during hydrogen charging (F$_{max}$ – tensile at fracture, l$_{fracture}$ – elongation at fracture, σ$_m$ =F$_{max}$/tensile specimen cross section in the notch)

	σ$_m$ (MPa)	l$_{fracture}$ (mm)	HEI (σ)	HEI (l)

8

E_{1-air}	1955.1±18.5	1.34±0.04	0.70±0.02	0.66±0.03
E_{1-H}	580.8±39.0	0.45±0.02		
E_{2-air}	2072.0±56.7	1.34±0.04	0.69±0.07	0.64±0.05
E_{2-H}	642.6±125.2	0.48±0.06		
E_{3-air}	1380.6±16.7	1.11±0.01	0.24±0.03	0.42±0.03
E_{3-H}	1043.0±34.8	0.64±0.04		
E_{4-air}	1337.6±5.2	1.06±0.1	0.21±0.04	0.39±0.07
E_{4-H}	1057.3±53.6	0.65±0.0		

HEI increases with increasing UTS in the air, the latter being predominantly the result of the tempering temperature - namely, higher tempering temperatures result in a lower UTS [34].

3.2. Fractographic and micro-CT analysis of the fracture surface following the SSRT tests

Larger ductile voids and quasi-cleavage facets were evident on the fracture surface of the E1 and E2 specimens tested in the air (Figure 3a, b, e and f). There were more quasi-cleavage facets in the fracture on the DCT specimen (E2 - Figure 3f) than in the CHT specimen (E1- Figure 3e). In comparison to E1 and E2, the fractures of E3 and E4 have finer ductile micro-voids (Figure 3c, d, g and h). The ductile micro-voids of the DCT specimen (E4 - Figure 3h), however, are coarser than those of the CHT specimen (E3 - Figure 3g).
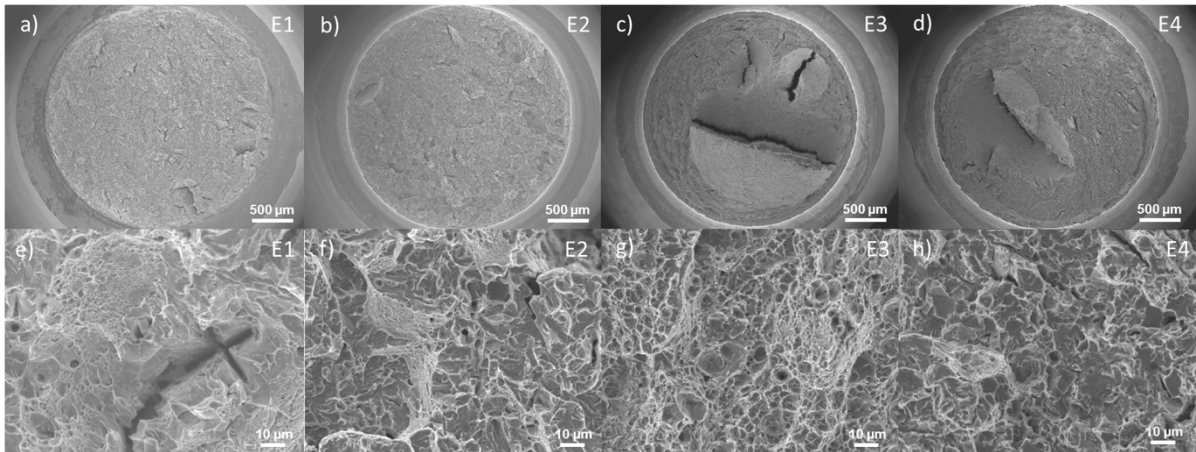
Figure 3: (a, b, c, d) respective SEM photos of the entire fracture surfaces of specimens E1 to E4 tested in the air (magnification 33 ×), and (e, f, g h) fracture surfaces at the edge of the specimens (magnification 1000 ×) for specimens E1 to E4, respectively

In the hydrogen-charged specimens, micro-void coalescence (MVC) is present in the center of the fractured surface, as shown within the circles in Figure 4a-d, outlined with dotted red lines. The area of ductile fracture is larger in the specimens hardened at a low austenitizing temperature and tempered at a high temperature (specimens E3 and E4, shown in Figure 4c and d), where the tensile strength and hardness before hydrogen charging is lower than that of the specimens austenitized at a high temperature and tempered at low temperatures (specimens E1 and E2, shown in Figure 4a and b).

The outer zones of specimens E1 and E2 (Figure 4e and f), outside the area outlined in red, are larger than in specimens E3 and E4, which is probably associated with the diffusion of hydrogen. In both sets of specimens, the outer zone consists of quasi-cleavage features (QC) and intergranular (IG) cracks between the prior austenite grains. Intergranular cracks, some wide open, were observed on all specimens tested during hydrogen charging (Figure 4e-h). This zone of fracture was hydrogen-assisted. The fractured facets of specimens E1 and E2, located in the hydrogen-assisted region, were coarser than the surfaces of specimens E3 and E4 - previous research suggests this is a consequence of the larger prior austenite grains and coarser martensite laths in the specimens E1 and E2 [11].

Based on the appearance of the fracture, and taking into consideration the high local stress near the V-notch where the crack is initiated and propagated, it is very likely that the dominant mechanism of fracture for the first set of specimens (E1 and E2) is HEDE. This can be explained by the influence of tempering temperature on strength (with a higher tempering temperature lowering the strength) [14,35,36]. According to Oriani's theory [20], the hydrostatic stress that exists in front of the notch crack defines the equilibrium hydrogen concentration that can be attained in front of the opened crack tip. A higher yield strength results in a higher hydrostatic stress and consequently a higher hydrogen concentration in front of the crack tip. Additionally, lower tempering temperatures do not allow sufficient relaxation of the quenched microstructure. The remains of structural defects on prior austenite grain boundaries can accumulate a higher amount of hydrogen atoms, causing their decohesion [37]. In the case of the second set of specimens (E3 and E4), which were tempered at a higher temperature, decohesion of the grain boundaries was evident but no further plasticity-related fracture facets were observed [36].
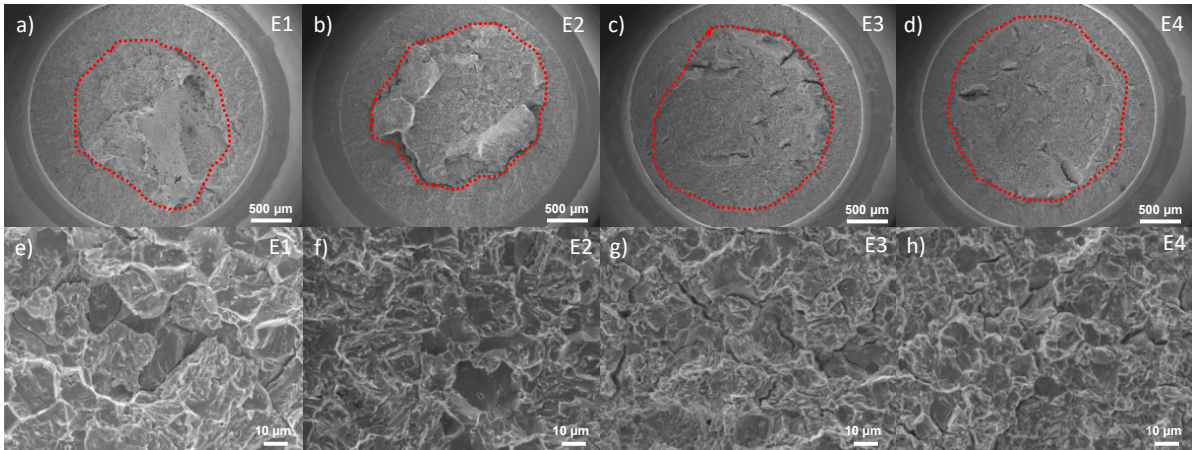
Figure 4: (a, b, c, d) SEM photos of the whole fractured surfaces of specimens E1 to E4, respectively, during hydrogen charging (magnification 33 ×), and (e, f g, h) the fractured surfaces at the edge of the specimens (magnification 1000 ×), in specimens E1 to E4, respectively)

MicroCT analysis of the fractured sections of the E1 material was performed on one specimen tested in the air (Figure 5a and b) and one specimen tested during hydrogen charging (Figure 5c and d). It can be seen from this analysis that no secondary cracks were present when the SSRT test was conducted in the air (Figure 5b), whereas in the hydrogen-charged specimen several cracks penetrating the core of the tensile test specimen are visible after the fracture, mostly outside the hydrogen-assisted zone. It can be concluded from these results that a single crack propagated within the zone of hydrogen diffusion during the SSRT tests, indicating high brittleness in this part of the fracture. Beyond this area, crack branching was observed (Figure 5d).

E1 – air testing, top view a)

E1 – air testing, cracks only b)

1 mm

1 mm

E1 – hydrogen charging, top view c)

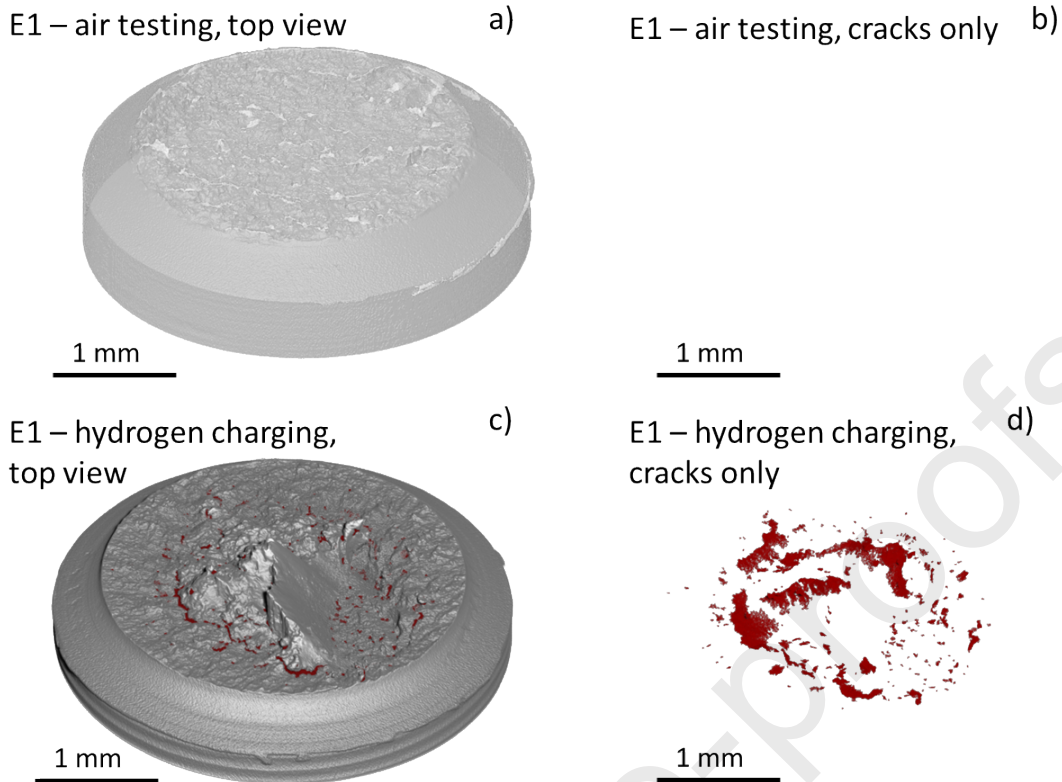E1 – hydrogen charging, cracks only d)

1 mm

1 mm

Figure 5: MicroCT scans imaging the upper surface of the fractured end of the E1 specimen tested a) in the air and c) during hydrogen charging, with a visualization of the cracks (marked in red) for the same specimen tested b) in the air (no propagation of secondary cracks observed) and d) during hydrogen charging

3.3. EBSD analysis of cracked specimens exposed to hydrogen charging

According to previous research [3], specimen E1 had the highest RA volume, at 15%. Figure 6a shows an EBSD phase map of this sample. At a lower magnification, a high presence of the austenitic, fcc phase (marked in green) can be observed in the lower part of the image, away from the propagating crack. Enlarging the region, as shown in Figure 6b, reveals only a few small islands of the austenitic phase. Corresponding IPF+IQ maps of this specimen, presented in Figure 6c and d, show randomly oriented fine martensitic laths, interrupted with elongated, banded delta ferrite bands with thicknesses of up to 30 μm. The cracks cross the bands of delta ferrite and do not appear to progress along them. The opposite, however, was observed in specimen E2, as can be seen in Figure 7. Similar to the E2 specimen, cracks in the E3 specimen propagate along the banded delta ferrite (Figure 8), with a few small RA islands present on the walls surrounding the crack. In this specimen the delta ferrite is also elongated, but it is thinner than it is in specimen E2.
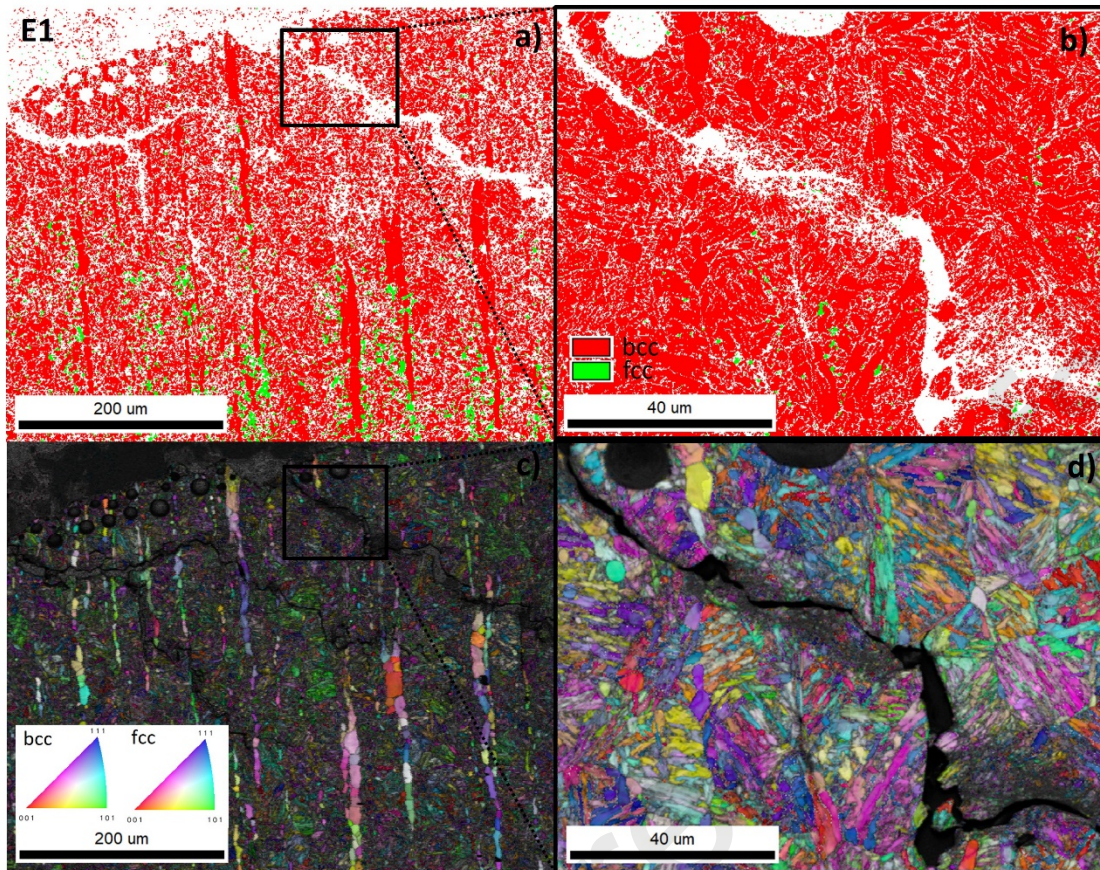
Figure 6: EBSD phase maps of cracks in the axial plane of steel specimen E1, shown at different magnifications (a and b); bcc phase (red) - martensite and delta ferrite; fcc phase (green) – austenite; and the corresponding IPF+QI maps (c and d). The fracture is at the top.
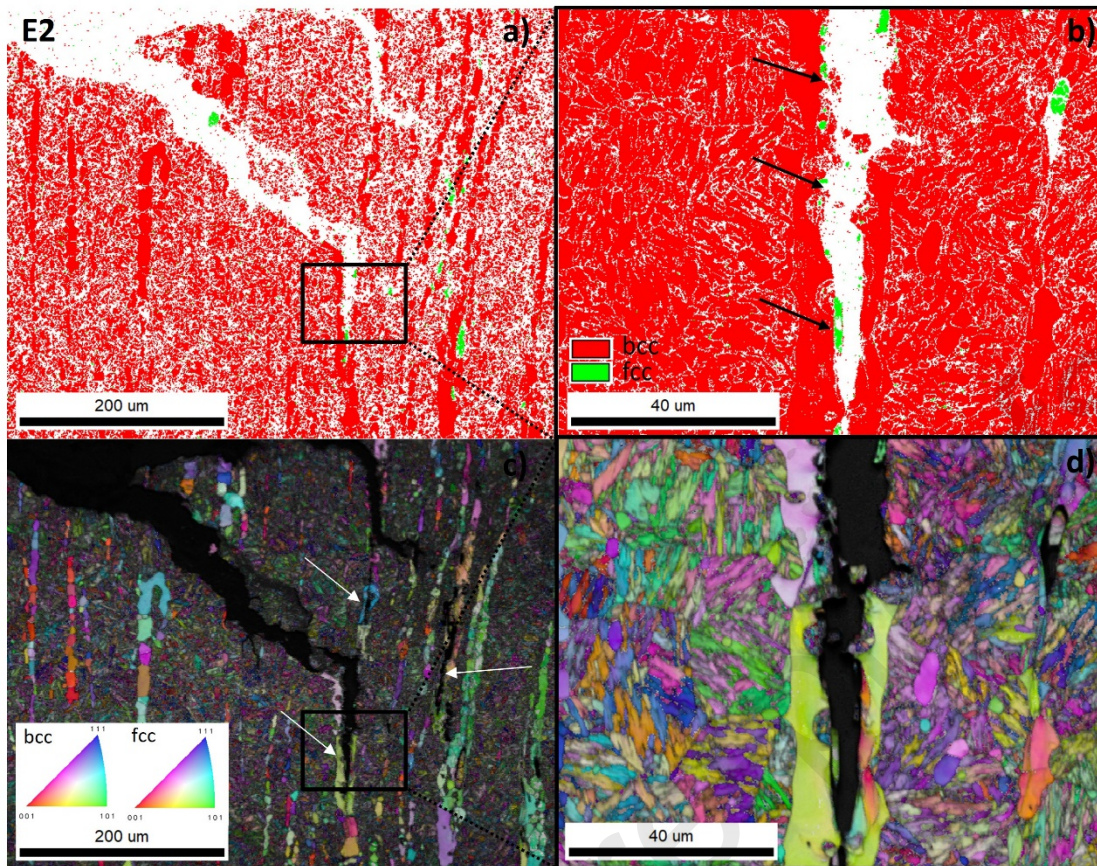
Figure 7: EBSD phase maps of cracks in the axial plane of steel specimen E2, shown at different magnifications (a and b); bcc phase (red) - martensite and delta ferrite; fcc phase (green) – austenite; and the corresponding IPF+QI maps (c and d). The fracture is at the top.
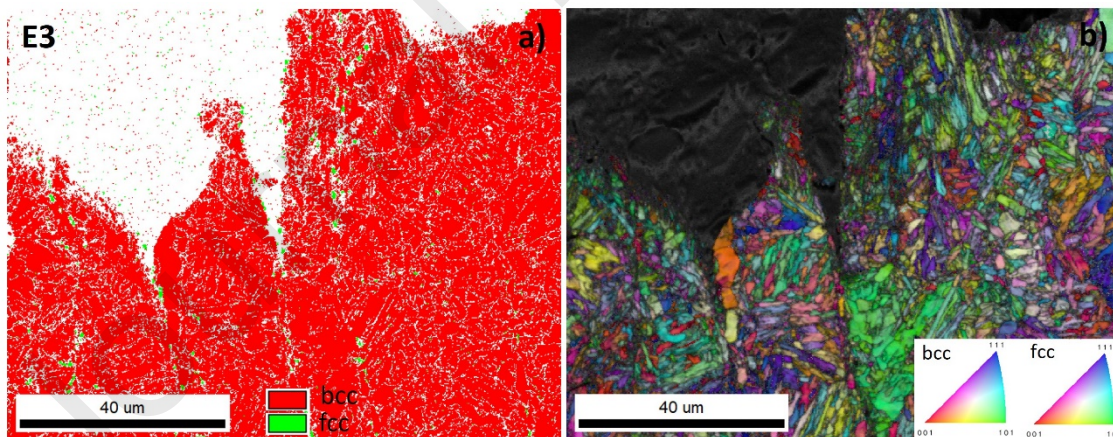

Figure 8: EBSD phase maps of the axial plane of the E3 specimen containing the phases bcc (red) - martensite and delta ferrite, and fcc (green) – austenite (a), and the corresponding IPF+QI maps (b). The fracture is at the top.

A characteristic crack in specimen E4 is presented in Figure 9a (phase map) and b (IPF+IQ map). The crack occurs at the tip, which is blunt, and is surrounded by delta ferrite (Figure 9b). Here some fine RA is also observed at the crack wall.
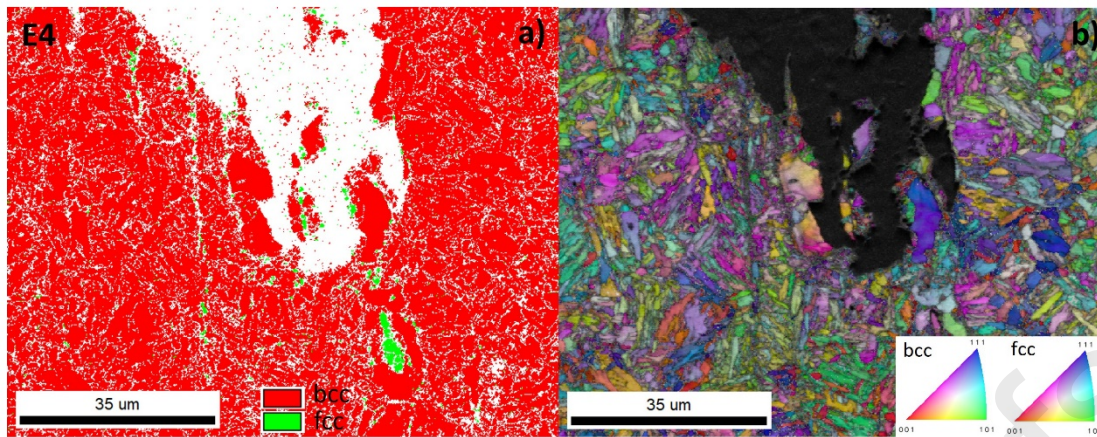
Figure 9: (a) EBSD phase maps of the axial plane in the E4 specimen, containing the phases bcc (red) - martensite and delta ferrite and fcc (green) – austenite, and (b) the corresponding IPF+QI maps. The fracture is at the top.

Based on the results of the SSRT tests, it can be concluded that DCT does not have a significant effect on the mechanical properties measured during hydrogen charging when compared to CHT. This is true for both groups of the material, which differ with respect to the temperature of austenitization. This finding is consistent with some sources in the literature [21], but contradicts others that have reported RA to have a beneficial effect on HE resistance [30]. Other studies have, however, indicated a detrimental effect [26]. The lack of RA near the V-notch in specimen E1, particularly around the propagating cracks, as evident in the EBSD images (Figure 6), could be explained by the transformation of RA into strain-induced martensite, due to the instability of the austenitic phase [27,29,38]. Despite this observation in the E1 specimen, the HE susceptibility of this specimen, in terms of HEI and fracture appearance, did not significantly differ from specimen E2, which had a far lower amount of RA before testing. Although hydrogen diffusion rate and solubility tests were not carried out within this investigation, the hydrogen diffusion coefficients of set E1-E2 and set E3-E4 can be compared based on the fracture analysis (Figure 4). As previously observed, the outer zone (the outer red line in Figures 4a-d) reaches deeper into the specimen in E1 and E2, indicating a deeper ingress of the hydrogen. When also taking into account the shorter charging time (a shorter time to fracture, see Figure 2) in these specimens, it becomes evident that the hydrogen diffusion coefficient in E1 and E2 is higher than that in E3 and E4. This contradicts the results of Zafra et.al. [14], who found that a higher tempering temperature led to a higher hydrogen diffusion coefficient - in our case, however, not only the tempering temperature but also the austenitizing temperature was varied. Consequently, different microstructures are formed, varying in terms of the appearance of martensite laths, prior austenite grain size and boundaries, carbides type, size and precipitation intensity, dislocation density and banded delta ferrite [39–41], etc… The higher HE susceptibility in the first set of specimens (E1 and E2) can be attributed to the higher tensile strength, resulting from both the difference in heat treatment temperatures as well as from the differences in microstructure previously mentioned. One of the most obvious differences between the specimens tested is their microstructures, as reported by Jovičević-Klug [3,11]: specimens E1 and E2 have coarser martensitic laths, whilst the microstructure of specimens E3 and E4 is finer. A higher tempering temperature results in more tempered martensite, with finer laths and larger carbides, and consequently a lower hardness [42]. Another obvious difference that can contribute to the HE susceptibility of the steels investigated is the amount of carbides [3,11]. Namely, it has been reported that the solubility of hydrogen increases in the presence of carbides [26]. In the present study, a higher amount of precipitates was observed in the first set of specimens (E1 and E2) than in the second (E3 and E4), but the difference between the total amount of carbides in E1 and E2 (23 and 25 vol%, respectively) and E3 and E4 (17 and 19.5 vol%, respectively) was not significant.

The present study indicates no influence of RA on HE susceptibility, but irrespective of the results it is important to consider that V-notch specimens yield different outcomes to smooth specimens, arising from differences in the concentration and distribution of stress [36].

4. Conclusion

In this work, we compared the impact of hydrogen charging on the mechanical properties of X17CrNi16-2 martensitic stainless steel, treated using either conventional heat treatment or deep cryogenic treatment.

Based on the results of the slow strain rate test during hydrogen charging, and observation of the final fracture, we can draw the following conclusions:

- Deep cryogenic treatment combined with heat treatment consisting of a high austenitizing temperature (1050 °C) and low tempering temperature (480 °C) reduces the amount of austenite retained in the microstructure [3,11]; no impact, either positive or negative, on the material's resistance to hydrogen embrittlement, was, however, observed.
- The effect of hydrogen was more detrimental in the first set of specimens i.e. the steels heat-treated at a high austenitizing temperature (1050 °C) and low tempering temperature (480 °C), where a 70% reduction in tensile strength was observed; steels heat treated at a lower austenitizing temperature (980 °C) and higher tempering temperature (600 °C), on the other hand, only exhibited a 30% reduction in tensile strength. The primary reason for this is most probably the finer lath microstructure of the latter specimens, which slows the diffusion of hydrogen.
- It can be concluded from results of the electron back-scatter diffraction analysis that, in the case of specimen E1 (conventionally heat-treated at a high austenitizing temperature [1050 °C] and low tempering temperature [480 °C]), which contained 15% of retained austenite, the austenite retained near the propagating cracks was transformed to deformation-induced martensite during the SSRT test.
- It is believed that, in all the specimens investigated, the most probable mechanism of hydrogen-assisted cracking is hydrogen-enhanced decohesion, caused by the high stress intensity near the V-notch in the tensile test specimens.

Author contributions

M. Bajt Leban: Formal Analysis, Writing (Original Draft, Review & Editing), Data/evidence collection, **B.Zajec:** Formal Analysis, Writing (Original Draft, Review & Editing), Data/evidence collection, **B. Podgornik:** Writing (Review & Editing), Funding Acquisition, **Č. Donik:** Formal Analysis, Writing (Original Draft), Data/evidence collection, **P. Jovičević-Klug:** Heat Treatment & Sample Preparation, Pre-Analysis, Writing (Original Draft, Review & Editing), **M. Hren**: Writing (Original Draft), Data/evidence collection, **A. Legat**: Writing (Review & Editing), Funding Acquisition

Data availability

The data that support the findings of this study are available from the corresponding authors upon reasonable request.

5. References

[1]   J.R. Davis, ASM International, eds., Stainless steels, ASM International, Materials Park, Ohio, 1994.

[2]   W.E. Bryson, Heat Treatment: Master Control Manual, Hanser, München, 2015.

[3]   P. Jovičević-Klug, M. Jovičević-Klug, T. Sever, D. Feizpour, B. Podgornik, Impact of steel type, composition and heat treatment parameters on effectiveness of deep cryogenic treatment, Journal of Materials Research and Technology 14 (2021) 1007–1020. https://doi.org/10.1016/j.jmrt.2021.07.022.

[4]   R.F. Barron, Cryogenic treatment of metals to improve wear resistance, Cryogenics 22 (1982) 409–413. https://doi.org/10.1016/0011-2275(82)90085-6.

[5]   F. Meng, K. Tagashira, R. Azuma, H. Sohma, Role of Eta-carbide Precipitations in the Wear Resistance Improvements of Fe-12Cr-Mo-V-1.4C Tool Steel by Cryogenic Treatment., ISIJ International 34 (1994) 205–210. https://doi.org/10.2355/isijinternational.34.205.

[6]   V.G. Gavriljuk, W. Theisen, V.V. Sirosh, E.V. Polshin, A. Kortmann, G.S. Mogilny, Yu.N. Petrov, Ye.V. Tarusin, Low-temperature martensitic transformation in tool steels in relation to their deep cryogenic treatment, Acta Materialia 61 (2013) 1705–1715. https://doi.org/10.1016/j.actamat.2012.11.045.

[7]   M. Villa, K. Pantleon, M.A.J. Somers, Evolution of compressive strains in retained austenite during sub-zero Celsius martensite formation and tempering, Acta Materialia 65 (2014) 383–392. https://doi.org/10.1016/j.actamat.2013.11.007.

[8]   D. Li, W. He, X. Zhang, M. Xiao, S. Li, K. Zhao, M. Yang, Effects of traditional heat treatment and a novel deep cryogenic treatment on microstructure and mechanical properties of low-carbon high-alloy martensitic bearing steel, J. Iron Steel Res. Int. 28 (2021) 370–382. https://doi.org/10.1007/s42243-020-00527-5.

[9]   P. Jurči, I. Dlouhý, Cryogenic Treatment of Martensitic Steels: Microstructural Fundamentals and Implications for Mechanical Properties and Wear and Corrosion Performance, Materials 17 (2024) 548. https://doi.org/10.3390/ma17030548.

[10]   W. Wang, V. Srinivasan, R. Siva, B. Albert, M. Lal, A. Alfantazi, Corrosion behavior of deep cryogenically treated AISI 420 and AISI 52100 steel, Corrosion 70 (2014) 708–720. https://doi.org/10.5006/1150.

[11]   P. Jovičević-Klug, M. Jovičević-Klug, L. Thormählen, J. McCord, M. Rohwerder, M. Godec, B. Podgornik, Austenite reversion suppression with deep cryogenic treatment: A novel pathway towards 3rd generation advanced high-strength steels, Materials Science and Engineering: A 873 (2023) 145033. https://doi.org/10.1016/j.msea.2023.145033.

17

[12] Y. Murakami, Metal fatigue: effects of small defects and nonmetallic inclusions, 2nd edition, Elsevier, Waltham, MA, 2019.

[13] M. Nagumo, Fundamentals of hydrogen embrittlement, Springer Berlin Heidelberg, New York, NY, 2015.

[14] A. Zafra, L.B. Peral, J. Belzunce, C. Rodríguez, Effects of hydrogen on the fracture toughness of 42CrMo4 steel quenched and tempered at different temperatures, International Journal of Pressure Vessels and Piping 171 (2019) 34–50. https://doi.org/10.1016/j.ijpvp.2019.01.020.

[15] M.B. Djukic, G.M. Bakic, V. Sijacki Zeravcic, A. Sedmak, B. Rajicic, The synergistic action and interplay of hydrogen embrittlement mechanisms in steels and iron: Localized plasticity and decohesion, Engineering Fracture Mechanics 216 (2019) 106528. https://doi.org/10.1016/j.engfracmech.2019.106528.

[16] X. Li, X. Ma, J. Zhang, E. Akiyama, Y. Wang, X. Song, Review of Hydrogen Embrittlement in Metals: Hydrogen Diffusion, Hydrogen Characterization, Hydrogen Embrittlement Mechanism and Prevention, Journal of Semiconductors 33 (2020) 759–773. https://doi.org/10.1007/s40195-020-01039-7.

[17] S. Lynch, Hydrogen embrittlement phenomena and mechanisms, Corrosion Reviews 30 (2012). https://doi.org/10.1515/corrrev-2012-0502.

[18] O. Barrera, D. Bombac, Y. Chen, T.D. Daff, E. Galindo-Nava, P. Gong, D. Haley, R. Horton, I. Katzarov, J.R. Kermode, C. Liverani, M. Stopher, F. Sweeney, Understanding and mitigating hydrogen embrittlement of steels: a review of experimental, modelling and design progress from atomistic to continuum, J Mater Sci 53 (2018) 6251–6290. https://doi.org/10.1007/s10853-017-1978-5.

[19] P.C. Okonkwo, E.M. Barhoumi, I. Ben Belgacem, I.B. Mansir, M. Aliyu, W. Emori, P.C. Uzoma, W.H. Beitelmal, E. Akyüz, A.B. Radwan, R.A. Shakoor, A focused review of the hydrogen storage tank embrittlement mechanism process, International Journal of Hydrogen Energy 48 (2023) 12935–12948. https://doi.org/10.1016/j.ijhydene.2022.12.252.

[20] R.A. Oriani, The diffusion and trapping of hydrogen in steel, Acta Metallurgica 18 (1970) 147–157. https://doi.org/10.1016/0001-6160(70)90078-7.

[21] L. Bacchi, F. Biagini, S. Corsinovi, M. Romanelli, M. Villa, R. Valentini, Influence of Thermal Treatment on SCC and HE Susceptibility of Supermartensitic Stainless Steel 16Cr5NiMo, Materials 13 (2020) 1643. https://doi.org/10.3390/ma13071643.

[22] G. Lovicu, E. Paravicini Bagliani, M. De Sanctis, A. Dimatteo, R. Ishak, R. Valentini, Hydrogen embrittlement of a medium carbon Q&P steel, Metallurgia Italiana 105 (2013) 3–10.

[23] J. Yang, F. Huang, Z. Guo, Y. Rong, N. Chen, Effect of retained austenite on the hydrogen embrittlement of a medium carbon quenching and partitioning steel with refined microstructure, Materials Science and Engineering: A 665 (2016) 76–85. https://doi.org/10.1016/j.msea.2016.04.025.

[24] J. Lee, T. Lee, D.-J. Mun, C.M. Bae, C.S. Lee, Comparative study on the effects of Cr, V, and Mo carbides for hydrogen-embrittlement resistance of tempered martensitic steel, Sci Rep 9 (2019) 5219. https://doi.org/10.1038/s41598-019-41436-2.

[25] J. Pešička, R. Kužel, A. Dronhofer, G. Eggeler, The evolution of dislocation density during heat treatment and creep of tempered martensite ferritic steels, Acta Materialia 51 (2003) 4847–4862. https://doi.org/10.1016/S1359-6454(03)00324-0.

[26] K.G. Solheim, J.K. Solberg, J. Walmsley, F. Rosenqvist, T.H. Bjørnå, The role of retained austenite in hydrogen embrittlement of supermartensitic stainless steel, Engineering Failure Analysis 34 (2013) 140–149. https://doi.org/10.1016/j.engfailanal.2013.07.025.

[27] Y.H. Fan, B. Zhang, H.L. Yi, G.S. Hao, Y.Y. Sun, J.Q. Wang, E.-H. Han, W. Ke, The role of reversed austenite in hydrogen embrittlement fracture of S41500 martensitic stainless steel, Acta Materialia 139 (2017) 188–195. https://doi.org/10.1016/j.actamat.2017.08.011.

[28] N. Narita, C.J. Altstetter, H.K. Birnbaum, Hydrogen-related phase transformations in austenitic stainless steels, Metall Trans A 13 (1982) 1355–1365. https://doi.org/10.1007/BF02642872.

[29] G. Álvarez, Z. Harris, K. Wada, C. Rodríguez, E. Martínez-Pañeda, Hydrogen embrittlement susceptibility of additively manufactured 316L stainless steel: Influence of post-processing, printing direction, temperature and pre-straining, Additive Manufacturing 78 (2023) 103834. https://doi.org/10.1016/j.addma.2023.103834.

[30] X. Li, J. Zhang, J. Chen, S. Shen, G. Yang, T. Wang, X. Song, Effect of aging treatment on hydrogen embrittlement of PH 13-8 Mo martensite stainless steel, Materials Science and Engineering: A 651 (2016) 474–485. https://doi.org/10.1016/j.msea.2015.09.116.

[31] B. Zhao, J. Song, L. Xie, Z. Hu, J. Chen, Surface roughness effect on fatigue strength of aluminum alloy using revised stress field intensity approach, Sci Rep 11 (2021) 19279. https://doi.org/10.1038/s41598-021-98858-0.

[32] X. Zhu, K. Zhang, W. Li, X. Jin, Effect of retained austenite stability and morphology on the hydrogen embrittlement susceptibility in quenching and partitioning treated steels, Materials Science and Engineering: A 658 (2016) 400–408. https://doi.org/10.1016/j.msea.2016.02.026.

[33] F. Aiello, M. Beghini, C.M. Belardini, L. Bertini, G. Macoretta, B.D. Monelli, R. Valentini, Proposal of a hydrogen embrittlement index for a martensitic advanced high-strength steel, Corrosion Science 222 (2023) 111357. https://doi.org/10.1016/j.corsci.2023.111357.

[34] B.S. Kumar, V. Kain, M. Singh, B. Vishwanadh, Influence of hydrogen on mechanical properties and fracture of tempered 13 wt% Cr martensitic stainless steel, Materials Science and Engineering: A 700 (2017) 140–151. https://doi.org/10.1016/j.msea.2017.05.086.

[35] M. Wang, E. Akiyama, K. Tsuzaki, Effect of hydrogen and stress concentration on the notch tensile strength of AISI 4135 steel, Materials Science and Engineering: A 398 (2005) 37–46. https://doi.org/10.1016/j.msea.2005.03.008.

[36] V. Arniella, A. Zafra, G. Álvarez, J. Belzunce, C. Rodríguez, Comparative study of embrittlement of quenched and tempered steels in hydrogen environments, International Journal of Hydrogen Energy 47 (2022) 17056–17068. https://doi.org/10.1016/j.ijhydene.2022.03.203.

[37] A. Zafra, L.B. Peral, J. Belzunce, C. Rodríguez, Effect of hydrogen on the tensile properties of 42CrMo4 steel quenched and tempered at different temperatures, International Journal of Hydrogen Energy 43 (2018) 9068–9082. https://doi.org/10.1016/j.ijhydene.2018.03.158.

[38] C.L. Lai, L.W. Tsay, C. Chen, Effect of microstructure on hydrogen embrittlement of various stainless steels, Materials Science and Engineering: A 584 (2013) 14–20. https://doi.org/10.1016/j.msea.2013.07.004.

[39] A. Lescur, E. Stergar, J. Lim, S. Hertelé, R.H. Petrov, Microstructural investigation and identification of intermetallic σ-phase in solution annealed 316L-type austenitic stainless steel, Materials Characterization 182 (2021) 111524. https://doi.org/10.1016/j.matchar.2021.111524.

[40] J. Michalska, B. Chmiela, Phase analysis in duplex stainless steel: comparison of EBSD and quantitative metallography methods, IOP Conf. Ser.: Mater. Sci. Eng. 55 (2014) 012010. https://doi.org/10.1088/1757-899X/55/1/012010.

[41] C.-C. Hsieh, W. Wu, Overview of Intermetallic Sigma (σ) Phase Precipitation in Stainless Steels, ISRN Metallurgy 2012 (2012). https://doi.org/10.5402/2012/732471.

[42] S.K. Bonagani, B. Vishwanadh, S. Tenneti, N. Naveen Kumar, V. Kain, Influence of tempering treatments on mechanical properties and hydrogen embrittlement of 13 wt% Cr martensitic stainless steel, International Journal of Pressure Vessels and Piping 176 (2019) 103969. https://doi.org/10.1016/j.ijpvp.2019.103969.

Highlights

- Conventionally and deep cryogenic treated martensitic stainless steel investigation
- Hydrogen influence on martensitic stainless steels mechanical properties
- Decreased fracture toughness in air of deep cryogenic treated steel
- No impact of deep cryogenic treatment on hydrogen charged specimens